

PAPER • OPEN ACCESS

Tuning the spintronic properties of graphene with atomically precise Au clusters

To cite this article: Wout Keijers *et al* 2021 *J. Phys. Mater.* **4** 045005

View the [article online](#) for updates and enhancements.

You may also like

- [Interaction of graphene with Au_n clusters: a first-principles study](#)
Ramasamy Murugesan, Ruishen Meng, Alexander de Volder et al.
- [Not so loosely bound rare gas atoms: finite-temperature vibrational fingerprints of neutral gold-cluster complexes](#)
Luca M Ghiringhelli, Philipp Gruene, Jonathan T Lyon et al.
- [SERRS and absorption spectra of pyridine on Au_mAg_n \(m + n = 6\) bimetallic nanoclusters: substrate composition and applied electric field effects](#)
Quanjiang Li and Maodu Chen



PAPER

OPEN ACCESS

RECEIVED

15 September 2021

ACCEPTED FOR PUBLICATION

23 September 2021

PUBLISHED

11 October 2021

Original Content from this work may be used under the terms of the [Creative Commons Attribution 4.0 licence](#).

Any further distribution of this work must maintain attribution to the author(s) and the title of the work, journal citation and DOI.



Tuning the spintronic properties of graphene with atomically precise Au clusters

Wout Keijers¹ , Ramasamy Murugesan² , Guillaume Libeert¹ , Jeroen E Scheerder¹ , Bart Raes¹, Steven Brems³ , Stefan De Gendt^{3,4} , Michel Houssa^{2,3}, Ewald Janssens¹ and Joris Van de Vondel^{1,*}

¹ Quantum Solid-State Physics, Department of Physics and Astronomy, KU Leuven, Celestijnenlaan 200D, B-3001 Leuven, Belgium

² Semiconductor Physics Laboratory, Department of Physics and Astronomy, KU Leuven, Celestijnenlaan 200D, B-3001 Leuven, Belgium

³ IMEC, Kapeldreef 75, 3001 Leuven, Belgium

⁴ Division of Molecular Design and Synthesis, Department of Chemistry, KU Leuven, Celestijnenlaan 200D, B-3001 Leuven, Belgium

* Author to whom any correspondence should be addressed.

E-mail: joris.vandevondel@kuleuven.be

Keywords: graphene, spintronics, metal clusters, spin-orbit coupling

Supplementary material for this article is available [online](#)

Abstract

Spin relaxation is investigated in lateral nonlocal graphene spin valves with increasing densities of soft-landed Au₃ and Au₆ clusters. It is found that both gold clusters scatter spins via the Elliot–Yafet mechanism. The induced spin–orbit coupling strength is a few meV for both clusters, with the value for Au₃ being roughly twice as large as that of Au₆. A gradual increase of the deposited cluster density (up to $\sim 10^{14}$ clusters cm⁻²) decreases the spin and momentum lifetime of the graphene channel, with Au₆ clusters affecting both spin and momentum lifetime more strongly than the Au₃ clusters. Density functional theory calculations provide insights into the spin relaxation mechanism. The dependence of graphene’s electronic and spintronic properties on the density and the exact cluster size indicates the importance of the microscopic details for graphene functionalisation towards spintronic applications.

1. Introduction

Graphene’s potential for spintronic applications has gained a lot of attention due to its gate tunability, high mobility, low hyperfine interactions, and its low intrinsic spin–orbit coupling (SOC) strength [1–4]. Researchers exploited these properties to propagate the electron spin up to 30 μm [5, 6]. Besides long distance spin communication, charge–spin conversion is essential to encode and process information in the spin degree of freedom [7–9]. Consequently, for an all-graphene based spintronic platform, control over the SOC is a necessary ingredient. Theoretical and experimental works indicate that strong Rashba spin–orbit coupling in graphene can be induced by the proximity effect. Transition metal dichalcogenides (TDMC’s) and adatoms have the potential to enhance the SOC [10–12], hereby inducing spin anisotropy [4, 13–15], enabling gate manipulation of spin transport [16, 17], induce a robust quantum spin Hall state [18], convert electrical current to spin current via the spin Hall effect (SHE) and vice-versa (iSHE) [19–22]. However, fundamental questions remain on the spin relaxation mechanisms in graphene. Both experimental and theoretical studies on the role of impurities and adatoms on the spin scattering yield contradictory results on the dominant spin scattering mechanism [23–27]. Moreover, in the case of adatom decorated graphene, recent theoretical studies highlight the importance of the microscopic details of these graphene–adatom interfaces. For example, *ab initio* calculations within the density functional theory framework showed that the induced SOC strongly depends on the adatom species and its exact position on the graphene lattice [28, 29]. Therefore, careful control on the atom-scale is an essential requirement in functionalizing graphene for spintronic properties.

In contrast to adatoms, cluster decoration allows not only to vary the elemental species, but also to tailor the cluster size. This additional degree of freedom provides a unique possibility to functionalize graphene.

State-of-the-art cluster fabrication and deposition techniques allow size and composition flexibility of clusters with atomic resolution as well as ultimate control of the deposition energy and density [30, 31]. Using these techniques, gas phase clusters showcased a distinct atom-by-atom size dependence, dominated by quantum confinement effects in the electronic and structural properties. This leads to unique physico-chemical properties, such as magnetic clusters made of atoms that form non-magnetic bulk metals [32] and catalytic activity of gold clusters opposed to their inert bulk phase [33–35]. Therefore, clusters can be considered an extension to the periodic table of elements in the third dimension [36]. These unique building blocks create a vast playground to modify graphene's electronic and spintronic properties.

Scheerder *et al* explored the electronic properties of graphene when decorated with few atom gold clusters [37, 38]. Size selected Au₃ and Au₆ clusters in an areal density range of 10¹³–10¹⁴ clusters cm⁻² were incrementally deposited on graphene, while its electrical properties were characterized. The electric properties of the hybrid material are dependent on the precise cluster sizes, including a size dependent doping efficiency. Moreover, DFT simulations showed that the triangular Au₆ cluster preferentially adsorbs parallel to the graphene with the gold atoms positioned above hollow sites of the hexagonal lattice, while the Au₃ cluster prefers to adsorb vertically with one Au atom above a C–C bridge. These size dependent structural differences make clusters unique adparticles to explore and control spin scattering in graphene for spintronic applications.

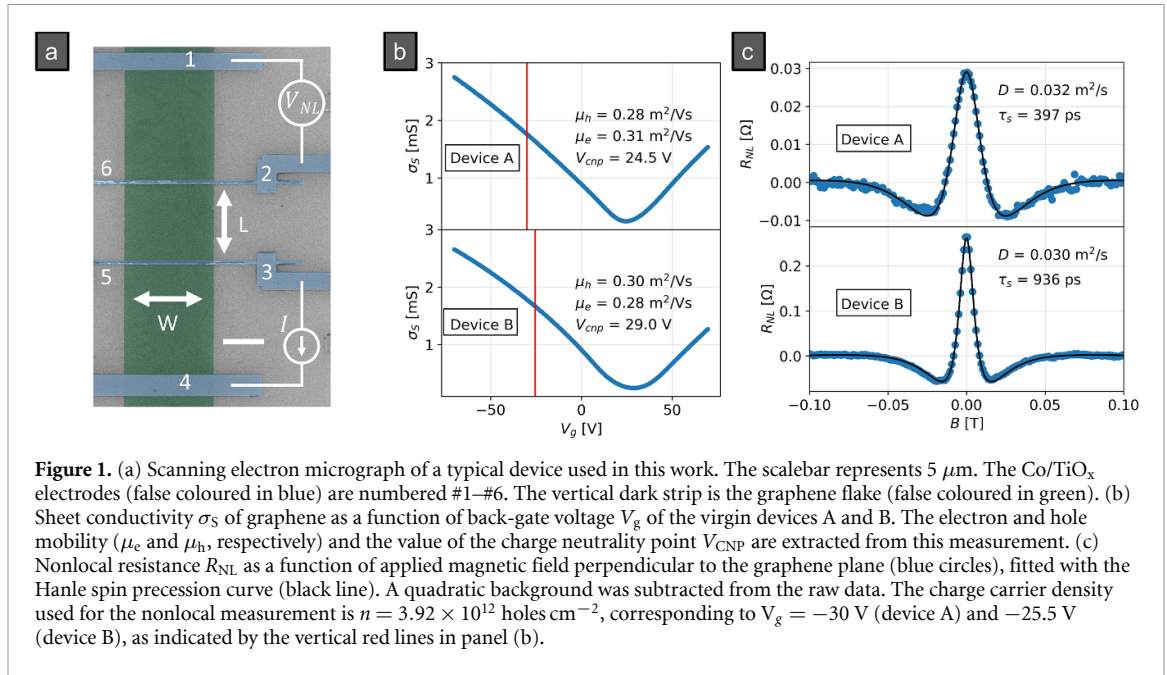
In this work, graphene's spin transport properties are studied at room temperature, while the Au cluster density is gradually increased. We show that Au₃ and Au₆ clusters deposited on graphene reduce the spin lifetime. However, at the same densities of deposited Au₃ and Au₆ clusters, the Au₆ reduces the spin lifetime to a greater extent. In particular, we observe that Au₆ is five times more effective as a spin scatterer and ten times as a momentum scatterer, in comparison to Au₃ clusters at the same deposited density. In the framework of Elliot–Yafet (EY) spin relaxation mechanism, the Au₃ cluster is observed to have a larger SOC compared to the Au₆ cluster. This dependence on cluster size highlights the importance of the microscopic details of the graphene-adparticle interaction. First-principles calculations performed in this work provide insights into these microscopic details. In these calculations, the SOC correspond to the experimentally obtained values.

2. Overview devices in their as-fabricated state

Graphene spin valves were fabricated to study the spintronic properties of graphene as a function of Au_{*n*} cluster density. A typical sample measured in this work is presented in figure 1(a). These spin valves consist of a $W = 10 \mu\text{m}$ wide graphene strip connected to six Co contacts (30 nm thick) separated by a 1 nm TiO_x barrier to mitigate the conductance mismatch [39, 40]. The inner electrodes contacting graphene are separated by $L = 10 \mu\text{m}$. The Co bars cover the full width of the graphene flake. One bar connects the numbered contacts from #2 and #6 and is 290 nm wide; the bar that connects #3 and #5 is 320 nm wide. The small width difference ensures a difference in coercivity in the easy magnetisation direction. The graphene layer resides on a highly doped Si⁺⁺ substrate terminated with a 300 nm SiO₂ top layer, which allows to control the carrier density using the ambipolar field effect [41]. The graphene is grown using platinum-based chemical vapor deposition (Pt-CVD) and subsequently transferred to the substrate [42]. In-house fabrication steps were performed using e-beam lithography and molecular beam epitaxy (MBE) deposition to nanopattern and metallize the spin valve. Fabrication details are summarized in the supplementary information (SI section 1) (available online at stacks.iop.org/JPMATER/4/045005/mmedia).

Two devices are discussed in this work: devices A and B. Device A has been decorated with Au₃ clusters, device B with Au₆ clusters. First, the virgin properties of both devices are examined, i.e. before cluster deposition. The sheet conductivity of both devices as a function of back-gate are presented in figure 1(b). The measurements were performed using a local four point probe measurement technique with a current of $I = 10 \mu\text{A}$. The current was applied from contact number #1 to #4, while voltage is measured over #2 and #3 (figure 1(a)). The density of charge carriers is calculated as $n = C_g(V_g - V_{\text{CNP}})$, with $C_g = 7.18 \times 10^{10} \text{ V}^{-1} \text{ cm}^{-2}$ resulting from the 300 nm SiO₂ dielectric, V_g the applied back-gate voltage and V_{CNP} the charge neutrality point. Similar virgin electronic properties (V_{CNP} and $\mu_{\text{h,e}}$) are found for samples A and B. The electron and hole mobilities were obtained from linear least-square fitting procedures in a 2 V interval around the steepest part of the conductivity curve $\sigma_S(V_g)$ [43, 44].

Figure 1(c) presents nonlocal Hanle spin precession measurements [45] of both graphene spin valves. A current of $I = 10 \mu\text{A}$ is applied from contacts numbered #4 to #3, while a nonlocal voltage V_{NL} is detected over contacts #1 and #2 (figure 1(a)). A magnetic field is applied perpendicular to the graphene plane. The nonlocal resistance is defined as $R_{\text{NL}} = V_{\text{NL}}/I$. Due to the square geometry of the graphene flake ($L/W = 1$), a significant background contribution to R_{NL} is observed [46]. Similar to Volmer *et al* [47], this background is asymmetric in the applied field and is attributed to inhomogeneous injection and detection of charges due



to pinholes in the 1 nm TiO_x barrier. The linear current-voltage relationship and the gate dependence of the nonlocal resistance ($R_{\text{NL}}(V_g)$) confirm the pinhole character of the TiO_x barrier [48]. Details can be found in the supplementary information (see SI section 3). This background was subtracted for all Hanle measurements.

In order to compare the spintronic properties of both devices, a back-gate voltage was applied at a constant voltage difference from the V_{CNP} to keep the charge carrier density constant. As a result, the Hanle spin precession measurements performed in this work are all obtained at a constant carrier density of $n = 3.92 \times 10^{12}$ holes cm^{-2} . The Hanle spin precession measurement is fitted to equation (1) originating from the 1D spin diffusion equation [45].

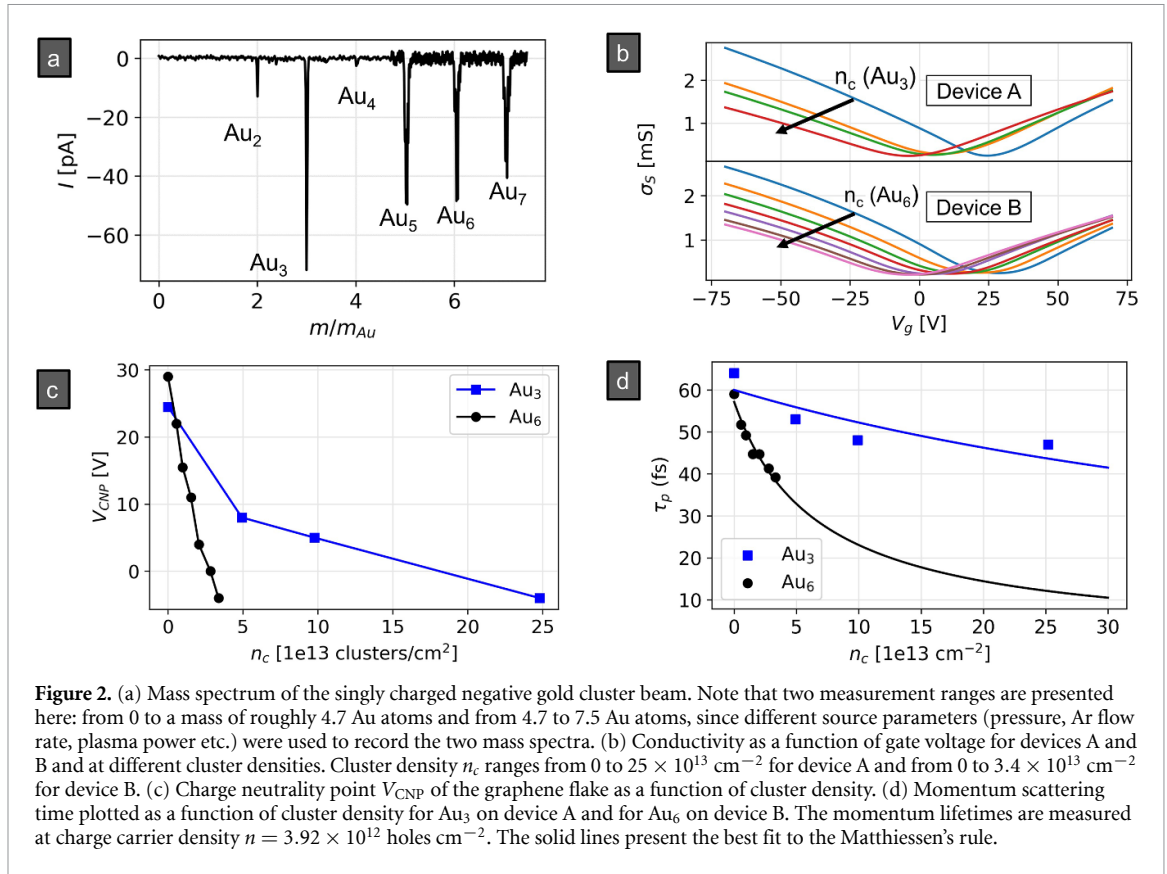
$$R_{\text{NL,Hanle}}(B) \propto \text{Re} \left\{ \frac{e^{-L\alpha}}{\alpha} \right\}, \quad (1)$$

where $\alpha = \sqrt{(1/\lambda_s)^2 + i(\omega/D)}$, with $\lambda_s = \sqrt{D\tau_s}$ the spin diffusion length and $\omega = g\mu_B B/\hbar$ the Larmor precession frequency induced by the applied magnetic field B . Here, D is the diffusion constant, τ_s the spin lifetime, g the electron g -factor, μ_B the Bohr magneton, and \hbar the reduced Planck's constant. The proportionality becomes an equality when the measured nonlocal signal R_{NL} is normalized to its value at zero magnetic field after background subtraction. The fitting procedure estimates the parameters τ_s and D for devices A and B. The spin lifetimes of the as-fabricated devices A and B are 397 ps and 936 ps, their diffusion constants are $0.032 \text{ m}^2 \text{ s}^{-1}$ and $0.030 \text{ m}^2 \text{ s}^{-1}$, respectively. The different lifetimes can be attributed to batch-to-batch variations in the fabrication process.

Due to a high correlation between the two fitting parameters, the relative (1-sigma) errors on the best fitting parameters τ_s and D are roughly 25% for device A and 10% for device B. These errors were obtained from the reduced $\chi^2 + 1$ (68% confidence) contour line in the (τ_s, D) -parameter space. Details on the fitting procedure are given in the supplementary information (SI section 3). The charge diffusion constant calculated using the Boltzmann formula [49] and Einstein equation matches well with the diffusion constant obtained from the Hanle fit ($D = 0.032 \text{ m}^2 \text{ s}^{-1}$ and $D = 0.031 \text{ m}^2 \text{ s}^{-1}$ for devices A and B at the doping level $n = 3.92 \times 10^{12}$ holes cm^{-2} , respectively). Next, the electronic properties of graphene are explored, while the cluster density is gradually increased.

3. Electronic properties of the gold cluster decorated graphene devices

The gold cluster production was performed using magnetron sputtering and inert gas condensation. Argon ions in a DC generated plasma sputter atoms from a gold target. These atoms cluster in the helium atmosphere of the condensation chamber and subsequently expand through an iris into vacuum forming a cluster beam. A quadrupole mass filter is able to size-select charged clusters with atomic precision. The

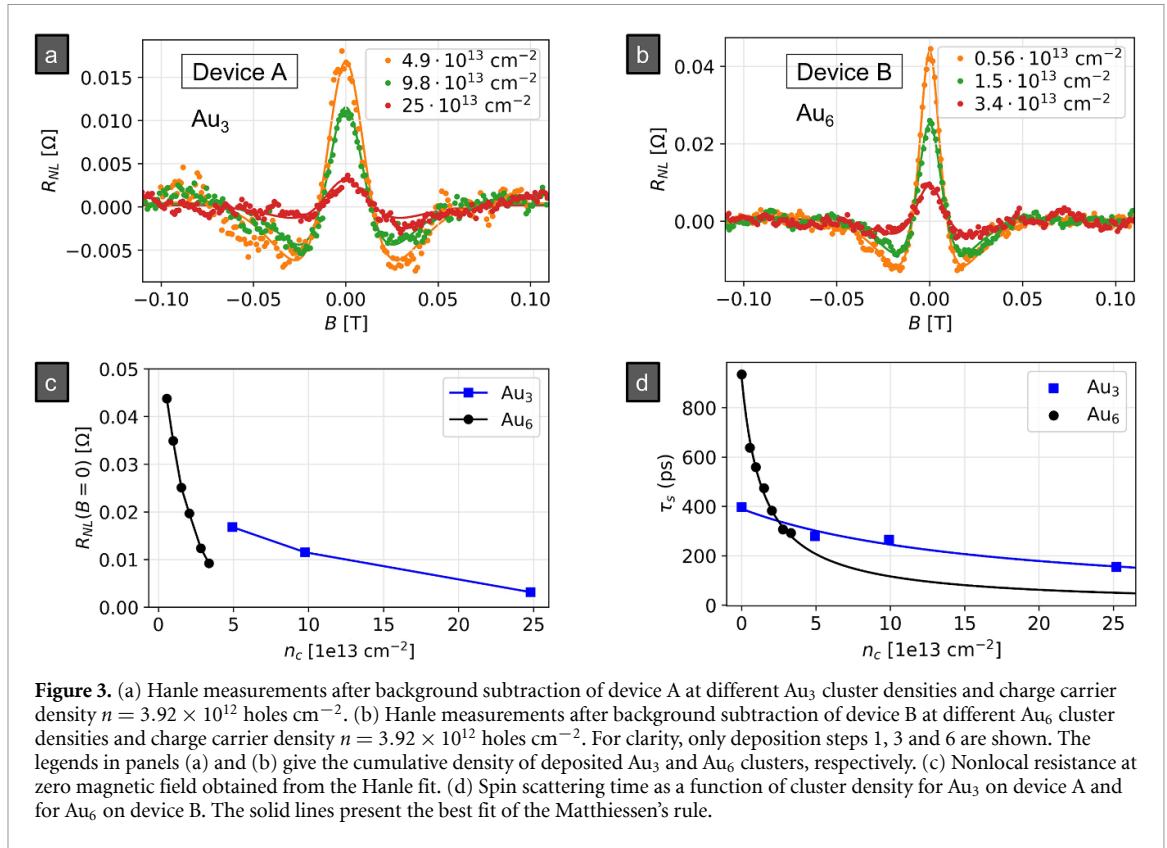


selected clusters are soft-landed ($\sim 1 \text{ eV atom}^{-1}$) on the microscopic graphene device [50]. During the complete experiment (multiple deposition and electrical characterization steps) the device is held in high vacuum ($\approx 10^{-8} \text{ mbar}$). Details of this apparatus can be found in [37].

Figure 2(a) presents the mass spectrum of the cluster beam before mass selection. It can be seen that a range of gold clusters can be created with the magnetron sputtering method. The total amount of clusters deposited on the device is monitored in real-time. Since all clusters arriving at the device carry a charge of $-1|e|$, the total amount of clusters landed is $|Q/e|$, where Q is the total charge obtained by taking the time integral of the current from the graphene device to ground during cluster deposition. Knowing the total area A of the device, the cluster density is $n_c = |Q/eA|$.

Figure 2(b) presents the conductivity measurements for devices A and B at different cluster densities. In the case of device A, it can be seen that the deposition of Au₃ up to a density $n_c = 25 \times 10^{13} \text{ cm}^{-2}$ decreases the V_{CNP} , while widening the valley of the conductivity curve. The same behaviour can be observed in the conductivity curve of device B. It is important to note that not only clusters of a different size were deposited on devices A and B, but that also the maximum density of deposited clusters is different. The cluster Au₆ density deposited on device B is an order of magnitude lower than the Au₃ density deposited on device A. The total Au₆ cluster density deposited on device B is $n_c = 3.4 \times 10^{13} \text{ cm}^{-2}$. The lower Au₆ cluster density was a necessary condition in order to have a measurable nonlocal spin resistance R_{NL} . The V_{CNP} as a function of cluster density is presented in panel (c). V_{CNP} decreases for both cluster sizes with n_c , indicating electron transfer from the cluster to the graphene [51]. It can be seen that Au₆ clusters cause a larger shift of V_{CNP} per density of added clusters compared to the Au₃ clusters. Using the cluster density and the shift in the charge neutrality point, the doping efficiency or number of electrons transferred from the cluster to graphene (or vice-versa) can be calculated [51]. The doping efficiency ε for Au₃ and Au₆ is 0.006 ± 0.001 electrons/cluster and 0.08 ± 0.02 electrons/cluster, respectively. These values correspond well with previous experimental observations by Scheerder *et al* [38].

To isolate the contribution of the cluster to the total momentum scattering in graphene, Matthiessen's rule is applied. Assuming there are two independent momentum scattering mechanisms: one due to the adsorbed clusters ($\tau_{\text{p,Au}_n}^{-1}$) and one umbrella term for all other possible scatterers in the virgin state ($\tau_{\text{p},0}^{-1}$), the total momentum scattering rate can be written as $\tau_{\text{p}}^{-1} = \tau_{\text{p,Au}_n}^{-1} + \tau_{\text{p},0}^{-1}$. Moreover, the cluster induced scattering rate is assumed to scale linearly with cluster density, i.e. $\tau_{\text{p,Au}_n}^{-1} = \Gamma_{\text{p,Au}_n} \cdot n_c$ with $\Gamma_{\text{p,Au}_n}$ the cluster



induced scattering rate per density of deposited clusters. The measured momentum scattering time and fit are presented in figure 2(d). The datapoints are calculated from the conductivity $\sigma(n)$ and charge carrier density $n = 3.92 \times 10^{12}$ holes cm^{-2} using the Boltzmann formalism. The best fit parameters are $\Gamma_{p,\text{Au}_3} = (2.5 \pm 1.2) \times 10^{-2} \text{ cm}^2 \text{ s}^{-1}$ and $\tau_{p,0} = 60$ fs for Au₃ on device A and $\Gamma_{p,\text{Au}_6} = (2.5 \pm 0.8) \times 10^{-1} \text{ cm}^2 \text{ s}^{-1}$ and $\tau_{p,0} = 57$ fs for Au₆ on device B. From these best fit parameters, it can be seen that the momentum scattering rate in the virgin state is similar for both devices. However, the induced rate Γ_{p,Au_n} due to the clusters is highly dependent on the cluster size, with a 10 times higher scattering rate per density for Au₆ as for Au₃. This large difference between the cluster sizes is compatible with charge impurity scattering theory [43, 52]: the Au₆ which has the largest doping efficiency also induces the largest scattering rates.

4. Spintronic properties of the gold cluster decorated graphene devices

Figure 3 presents the spintronic properties of devices A and B and their dependence on the Au₃ and Au₆ deposited cluster density. Figure 3(a) shows examples of Hanle measurements conducted after Au₃ cluster depositions on device A. Note that the shape of the curves are similar to those of the device before cluster deposition (figure 1(c)), but the maximum amplitude of the nonlocal resistance at zero magnetic field decreases after each cluster deposition step. Figure 3(b) presents the Hanle spin precession measurements at different Au₆ cluster densities on device B. Similar as for device A, an overall decrease in signal with n_c can be observed, while the shape of the curve is unaltered.

For the virgin and low cluster coverage measurements, the characteristic parameters of spin transport (τ_s, D) are obtained by fitting the data to equation (1). The spin lifetime at higher cluster density is extracted differently. Due to the lower signal to noise ratio (S/N) of the nonlocal resistance R_{NL} and the inherent correlation between the Hanle fitting parameters τ_s and D , the Hanle fitting method fails to extract these parameters reliably (see SI section 3). Therefore, an alternative method, discussed below, is applied for the higher cluster densities. The extracted spin lifetimes, for both methods, are presented in figure 3(d).

According to Takahashi *et al* [53], in the case for the intermediate regime in barrier resistances, the spin contribution to the nonlocal signal can be written as

$$\Delta R_{\text{NL}} = C\sigma_{\text{sf}}(\lambda_s), \quad (2)$$

with $\Delta R_{\text{NL}} = R_{\text{NL}}^{\text{P}} - R_{\text{NL}}^{\text{AP}}$, where P (AP) denotes the relative orientation of the center Co bar magnetization orientation as (anti)parallel. Furthermore,

$$C = \frac{4P_J^2}{(1 - P_J^2)^2} R_1 R_2 \frac{W}{L}, \quad f(\lambda_s) = \frac{L}{\lambda_s} \left[\frac{e^{-L/\lambda_s}}{1 - e^{-2L/\lambda_s}} \right], \quad (3)$$

where R_1 and R_2 are the barrier resistances and P_J is the geometric average of the injection and detection efficiency. As a result, the nonlocal spin signal ΔR_{NL} can be separated into the factor C , which only depends on device geometry, barrier resistance and spin injection/detection efficiency, σ_s the graphene sheet conductivity, and the function $f(\lambda_s)$, capturing the quality of the channel/medium through which the spin current propagates. The function f only depends on the length of the spin valve L and the spin diffusion length λ_s .

For the data presented in figure 3 panels (a)–(c), the barrier resistance remained constant, allowing us to compare the nonlocal resistance R_{NL} at zero field as an indicator for the quality of the graphene channel as a spin conductor. Using the λ_s obtained from the Hanle fits at low cluster densities, C is calculated with equation (2) for each device. Subsequently, equations (2) and (3) are used in the inverse direction at high cluster coverages to obtain the spin diffusion length λ_s from the amplitude of the nonlocal signal at zero magnetic field. For both devices A and B, the nonlocal resistance at zero magnetic field as a function of cluster density is plotted in panel (c). In combination with the diffusion constant $D = v_F^2 \tau_p / 2$, found from the electrical characterization, the spin lifetime $\tau_s = \lambda_s^2 / D$ is obtained (see figure 3(d)).

Similar to the Matthiessen's fit to the momentum relaxation time, the same procedure is applied to the spin scattering time, i.e. $\tau_s^{-1} = \tau_{s,\text{Au}_n}^{-1} + \tau_{s,0}^{-1}$ with $\tau_{s,\text{Au}_n}^{-1} = \Gamma_{s,\text{Au}_n} \cdot n_c$. In this manner, the cluster contribution to the spin scattering can be distinguished from the virgin scatterers. The result of the fitting are shown as the solid lines and result in a $\Gamma_{s,\text{Au}_3} = (1.5 \pm 0.5) \times 10^{-5} \text{ cm}^2 \text{ s}^{-1}$ and $\tau_{s,0} = 390 \text{ ps}$ for the Au_3 deposition on device A. Au_6 on device B produced $\Gamma_{s,\text{Au}_6} = (7.5 \pm 1.5) \times 10^{-5} \text{ cm}^2 \text{ s}^{-1}$ and $\tau_{s,0} = 924 \text{ ps}$. These fitted $\tau_{s,0}$'s compare perfectly with the spin lifetimes in the virgin state obtained from the Hanle fitting (figure 1(c)). The fitted Γ_s 's indicate the size-dependent properties of the two cluster sizes: Au_6 is five times more effective as a spin scatterer compared to the Au_3 cluster.

In summary, the experiments provide a clear difference between the induced momentum and spin scattering rates per density (Γ_{Au_n} 's) for the two cluster sizes examined. It is found that the Au_6 cluster is more effective in momentum scattering by a factor of ten, and in spin scattering with a factor of five compared to the Au_3 cluster. Next, to obtain insights in the spin–orbit coupling induced by the cluster, density functional theory simulations are carried out.

5. Density functional theory simulations

In addition to the experiments, first-principles calculations were performed based on density functional theory using the Vienna *ab initio* simulation package (VASP) with plane wave basis sets [54–57]. First, the most stable geometrical configuration for the graphene– Au_n ($n = 3, 6$) system was searched by relaxing the cluster in different orientations and at different adsorption sites on the graphene plane. It is found that the triangular Au_3 cluster prefers to adsorb on a C–C bridge position with C–Au bond lengths between the two nearest C atoms 2.25 Å and 2.5 Å. The triangular Au_6 cluster prefers a configuration parallel to the graphene plane. The stable geometry of the Au_6 cluster is adsorbed 3.5 Å above the graphene plane (see figure 4, panels (c) and (f)). The binding energy of Au_3 cluster on graphene is estimated to be -1.57 eV , while that of Au_6 cluster is -2.25 eV . These computational results indeed show the position of the bond is different for both cluster sizes. Details on these calculations can be found in the supplementary information (SI section 5).

Figures 4(a) and (d) present the band structures without spin-orbit interactions using a 5×5 graphene supercell with 50 carbon atoms ($n_c = 7.584 \times 10^{13} \text{ cm}^{-2}$) and one adsorbed Au_3 and Au_6 cluster, respectively. It can be seen that the valence Au 6s orbitals of the Au_3 cluster are energetically close to the Fermi level and strongly hybridize with the C p_z orbital. Furthermore, there is a band opening at Dirac point in graphene– Au_3 system. Strong orbital hybridization could be the reason for this gap opening. Taking into account the cluster density in this simulation, the shift of the Dirac point with respect to the Fermi level corresponds to a cluster doping efficiency of $\varepsilon = 0.062 \text{ e}/\text{cluster}$. For Au_6 clusters on the other hand, the Au valence orbitals are far from the Fermi level (panel (d) of figure 4). Here, it can be seen that the Au_6 cluster does not affect the Dirac cone by much near the Fermi level. Moreover, Au_6 adsorption does not shift the Fermi level with respect to the Dirac cone and therefore the Au_6 shows a negligible doping efficiency.

The experimental doping efficiencies are not reflected in the DFT calculations. Possible reasons for this mismatch could be due to (a part of) the clusters having a different geometry than what is considered in the

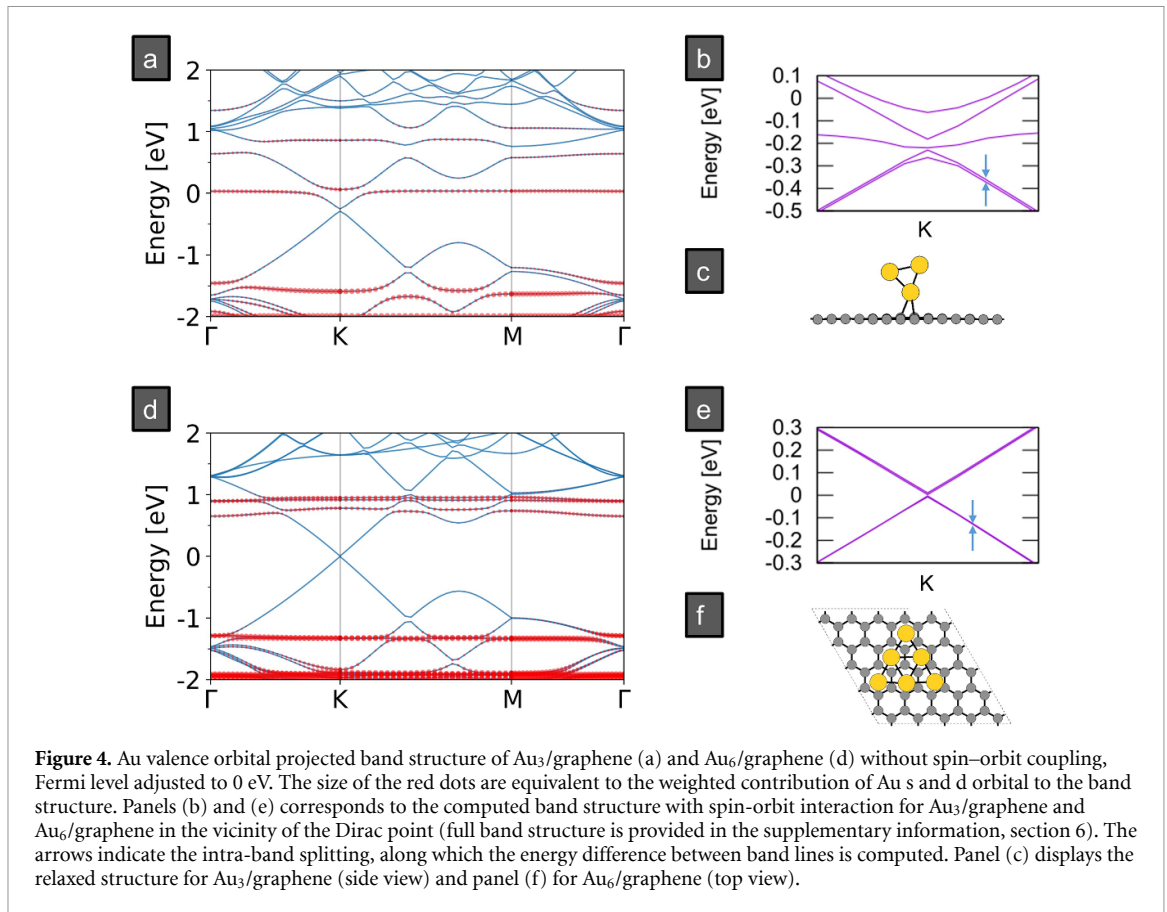


Figure 4. Au valence orbital projected band structure of Au₃/graphene (a) and Au₆/graphene (d) without spin-orbit coupling, Fermi level adjusted to 0 eV. The size of the red dots are equivalent to the weighted contribution of Au s and d orbital to the band structure. Panels (b) and (e) corresponds to the computed band structure with spin-orbit interaction for Au₃/graphene and Au₆/graphene in the vicinity of the Dirac point (full band structure is provided in the supplementary information, section 6). The arrows indicate the intra-band splitting, along which the energy difference between band lines is computed. Panel (c) displays the relaxed structure for Au₃/graphene (side view) and panel (f) for Au₆/graphene (top view).

DFT simulations, leading to a different interaction and doping efficiency, potentially mediated by the presence of defects/residues on graphene interacting with the cluster. Furthermore, we should keep in mind that we are simulating a free-standing perfect graphene layer interacting with Au_n clusters, which may be different from the transferred graphene layer on the Si/SiO₂ substrates.

Panels (b) and (e) present closer views at the Dirac cone, in this case including spin-orbit interactions, for adsorbed Au₃ and Au₆ clusters, respectively. Spin-orbit coupling lifts the degeneracy of spin states and causes band splitting. In graphene spin-orbit interaction opens up a gap in the Dirac cone. Weeks *et al* studied this SO induced gap for indium and thallium adatom coverage on graphene [18]. However, in the present work there is strong orbital hybridization between graphene and Au valence orbital, opening up a gap even in the absence of SO coupling. Marchenko *et al* observed a strong enhancement in the SO splitting for graphene covered by a graphene monolayer due to hybridization with Au 5d state [58]. They also observed a splitting of the Dirac cone of a few meV when the graphene sublattice is in top position with respect to the gold monolayer and estimated the SO splitting in the vicinity of the Dirac point along the band line. Marchenko *et al* estimated the SO splitting by calculating the absolute values of energy difference between band lines along valence band [59]. Therefore, to study and distinguish the SO induced splitting from orbital hybridization, intra-band splitting is measured along the band line away from the Dirac point ($\Gamma \rightarrow K$ and $K \rightarrow M$) as indicated by the arrows in panels (b) and (e).

The strength of the induced spin-orbit coupling with varying cluster density is studied by performing simulations on different sizes of graphene supercells (5×5 , 7×7 , 8×8 and 10×10 carbon atoms supercells) containing one Au₃ or Au₆ adsorbed cluster. The estimated SOC strength from the computed band structures are shown in figure 5, evaluated in a range of -0.1 eV to -0.6 eV below the Dirac point. The errorbars present the range in SOC in this energy interval. The SOC induced intra-band splitting is in the range of 4–13 meV for Au₃ and 2–5 meV for Au₆. So, also for the SOC a cluster size dependence is observed with Au₃ inducing a larger SOC. A SOC of the same order of magnitude (~ 10 meV) has been reported for Rashba SOC in graphene in contact with a full layer of Au atoms [58, 60]. Theoretical predictions also yield similar results for impurities on graphene [10]. Next, the DFT simulations are compared to the experimental observations.

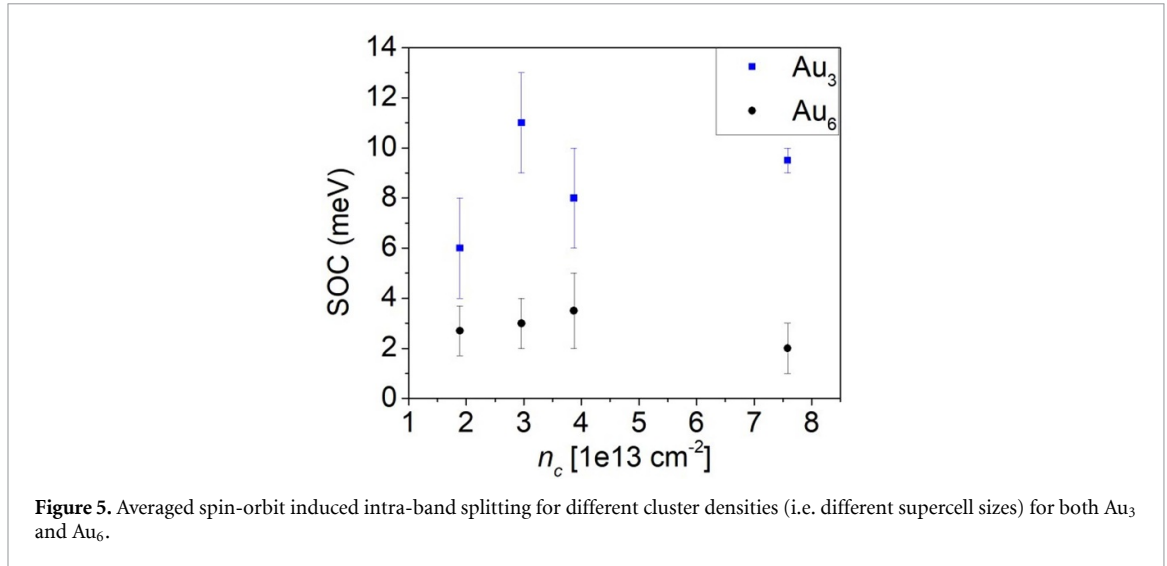


Figure 5. Averaged spin-orbit induced intra-band splitting for different cluster densities (i.e. different supercell sizes) for both Au₃ and Au₆.

6. Discussion

In order to compare the DFT results to the experiments, a specific spin scattering mechanism needs to be considered in order to extract a SOC energy from the experimentally obtained scattering lifetimes (τ_s and τ_p). In both devices, the spin lifetime decreases as the momentum scattering time is reduced, indicating an Elliot–Yafet (EY)-like [61, 62] spin scattering induced by the gold clusters. The spin scattering rate in the EY mechanism is $\tau_s^{-1} = \frac{\Delta_{\text{EY}}^2}{E_F^2 \tau_p}$. Note that the Fermi level $E_F = 0.231 \text{ eV}$ is constant in the experiment since the charge carrier density was fixed at $n = 3.92 \times 10^{12} \text{ holes cm}^{-2}$ by tuning the back-gate voltage. In order to extract the SOC induced by the clusters, the Matthiessen’s rule is applied as before to exclude the virgin state’s contribution. Therefore, $\tau_s^{-1} = \frac{\Delta_{\text{EY,Au}_n}^2}{E_F^2} \tau_{p,\text{Au}_n}^{-1} + \tau_{s,0}^{-1}$, with $\Delta_{\text{EY,Au}_n}$ the induced SOC by the gold cluster assuming the EY mechanism as the dominant spin relaxation mechanism and $\tau_{s,0}$ the spin lifetime in the virgin state. Rewriting this equation results in an EY SOC induced by the gold clusters

$$\Delta_{\text{EY,Au}_n} = E_F \sqrt{\Gamma_{s,\text{Au}_n} / \Gamma_{p,\text{Au}_n}}. \quad (4)$$

Using the fitted Γ_{s,Au_n} and Γ_{p,Au_n} , the $\Delta_{\text{EY,Au}_n}$ is found to be $(5.7 \pm 1.6) \text{ meV}$ and $(3.9 \pm 0.8) \text{ meV}$ for Au₃ and Au₆, respectively. As the EY SOC is related to a spin scattering probability at each momentum scattering event, a cluster density independent $\Delta_{\text{EY,Au}_n}$ is compatible with the EY theory [63]. Both the order of magnitude and the relative $\Delta_{\text{EY,Au}_n}$ strength of the Au₃ and Au₆ systems are consistent with the SOC extracted from the density functional theory simulations (see figure 5), which did not show a clear trend with the cluster density, further supporting the EY scattering mechanism.

In summary, a consistent cluster size dependence of the SOC is seen in experiment and DFT simulations. The SOC differs a factor of 2–3 in the simulations and about 40% in the experiments between Au₃ and Au₆ decorated graphene, with Au₃ inducing the largest value.

7. Conclusion

This work demonstrates the manipulation of spin currents using adsorbed size-selected Au clusters in a graphene spin valve. It was found that Au₆ clusters adsorbed on graphene are more effective momentum and spin scattering centres per density compared to Au₃ clusters. Guided by *ab initio* simulations, similar SOC values were found in the simulations assuming that Au_n clusters ($n = 3, 6$) scatter the diffusing spins through the Elliot–Yafet mechanism. Moreover, it is found that the adsorbed Au₃ cluster induces a stronger spin–orbit coupling in graphene than the adsorbed Au₆ cluster. This indicates the importance of the exact positioning of the adparticle on the graphene lattice as well as the strong size-dependent properties of the cluster. This approach not only provides insight into the spin relaxation mechanism, but opens possibilities to investigate the robust quantum Hall state and the (i)SHE towards spintronic applications.









Data availability statement

The data that support the findings of this study are available upon reasonable request from the authors.

Acknowledgments

This research has been supported by the Research Foundation-Flanders (FWO project G.0D56.19N) and by the KU Leuven Internal Research Fund C14/17/080.

ORCID iDs

Wout Keijers  <https://orcid.org/0000-0002-1133-6904>
Ramasamy Murugesan  <https://orcid.org/0000-0001-6294-7206>
Guillaume Libeert  <https://orcid.org/0000-0003-1392-5371>
Jeroen E Scheerder  <https://orcid.org/0000-0002-9301-0392>
Steven Brems  <https://orcid.org/0000-0002-0282-8528>
Stefan De Gendt  <https://orcid.org/0000-0003-3775-3578>
Ewald Janssens  <https://orcid.org/0000-0002-5945-1194>
Joris Van de Vondel  <https://orcid.org/0000-0001-6894-7258>

References

- [1] Fischer J, Trauzettel B and Loss D 2009 Hyperfine interaction and electron-spin decoherence in graphene and carbon nanotube quantum dots *Phys. Rev. B* **80** 155401
- [2] Min H, Hill J E, Sinitsyn N A, Sahu B R, Kleinman L and MacDonald A H 2006 Intrinsic and Rashba spin-orbit interactions in graphene sheets *Phys. Rev. B* **74** 165310
- [3] Yazyev O V 2008 Hyperfine interactions in graphene and related carbon nanostructures *Nano Lett.* **8** 1011–5
- [4] Antonio Benítez L, Sierra J F, Saverio Torres W, Arrighi A, Bonell F, Costache M V and Valenzuela S O 2018 Strongly anisotropic spin relaxation in graphene–transition metal dichalcogenide heterostructures at room temperature *Nat. Phys.* **14** 303–8
- [5] Gebeyehu Z M et al 2019 Spin communication over 30 μm long channels of chemical vapor deposited graphene on SiO_2 *2D Mater.* **6** 034003
- [6] Drögeler M et al 2016 Spin lifetimes exceeding 12 ns in graphene nonlocal spin valve devices *Nano Lett.* **16** 3533–9
- [7] Roche S et al 2015 Graphene spintronics: the European flagship perspective *2D Mater.* **2** 030202
- [8] Kasun P and Xuan P A G 2019 Tuning spin–orbit coupling in 2D materials for spintronics: a topical review *J. Phys.: Condens. Matter* **31** 193001
- [9] Avsar A, Ochoa H, Guinea F, Ozyilmaz B, van Wees B J and Vera-Marun I J 2019 *Colloquium*: spintronics in graphene and other two-dimensional materials *Rev. Mod. Phys.* **92** 21003
- [10] Castro Neto A H and Guinea F 2009 Impurity-induced spin-orbit coupling in graphene *Phys. Rev. Lett.* **103** 026804
- [11] Katoch J 2015 Adatom-induced phenomena in graphene *Synth. Met.* **210** 68–79
- [12] Ge J-L, Wu T-R, Gao M, Bai Z-B, Cao L, Wang X-F, Qin Y-Y and Song F-Q 2017 Weak localization of bismuth cluster-decorated graphene and its spin-orbit interaction *Front. Phys.* **12** 127210
- [13] Raes B, Scheerder J E, Costache M V, Bonell F, Sierra J F, Cuppens J, Van De Vondel J and Valenzuela S O 2016 Determination of the spin-lifetime anisotropy in graphene using oblique spin precession *Nat. Commun.* **7** 11444
- [14] Ghiasi T S, Ingla-Aynés J, Kaverzin A A and Van Wees B J 2017 Large proximity-induced spin lifetime anisotropy in transition-metal dichalcogenide/graphene heterostructures *Nano Lett.* **17** 7528–32
- [15] Bundesmann J, Kochan D, Tkatschenko F, Fabian J and Richter K 2015 Theory of spin-orbit-induced spin relaxation in functionalized graphene *Phys. Rev. B* **92** 081403
- [16] Dankert A and Dash S P 2017 Electrical gate control of spin current in van der Waals heterostructures at room temperature *Nat. Commun.* **8** 16093
- [17] Yan W, Txoperena O, Llopis R, Dery H, Hueso L E and Casanova F 2016 A two-dimensional spin field-effect switch *Nat. Commun.* **7** 13372
- [18] Weeks C, Hu J, Alicea J, Franz M and Wu R 2011 Engineering a robust quantum spin hall state in graphene via adatom deposition *Phys. Rev. X* **1** 021001
- [19] Ferreira A, Rappoport T G, Cazalilla M A and Castro Neto A H 2014 Extrinsic spin Hall effect induced by resonant skew scattering in graphene *Phys. Rev. Lett.* **112** 066601
- [20] Jia Z, Yan B, Niu J, Han Q, Zhu R, Yu D and Wu X 2015 Transport study of graphene adsorbed with indium adatoms *Phys. Rev. B* **91** 085411
- [21] Van Tuan D, Marmolejo-Tejada J M, Waintal X, Nikolić B K, Valenzuela S O and Roche S 2016 Spin Hall effect and origins of nonlocal resistance in adatom-decorated graphene *Phys. Rev. Lett.* **117** 176602
- [22] Safer C K et al 2019 Room-temperature spin Hall effect in graphene/MoS₂ van der Waals heterostructures *Nano Lett.* **19** 1074–82
- [23] Pi K, Wei Han K M, McCreary A G, Swartz Y Li and Kawakami R K 2010 Manipulation of spin transport in graphene by surface chemical doping *Phys. Rev. Lett.* **104** 187201
- [24] Józsa C, Maassen T, Popinciuc M, Zomer P J, Veligura A, Jonkman H T and Van Wees B J 2009 Linear scaling between momentum and spin scattering in graphene *Phys. Rev. B* **80** 241403(R)
- [25] Han W and Kawakami R K 2011 Spin relaxation in single-layer and bilayer graphene *Phys. Rev. Lett.* **107** 047207
- [26] Swartz A G, Chen J R, McCreary K M, Odenthal P M, Han W and Kawakami R K 2013 Effect of *in situ* deposition of Mg adatoms on spin relaxation in graphene *Phys. Rev. B* **87** 075455
- [27] Zhang P and Wu M W 2012 Electron spin relaxation in graphene with random Rashba field: comparison of the D'yakonov–Perel' and Elliott–Yafet-like mechanisms *New J. Phys.* **14** 033015
- [28] Pachoud A, Ferreira A, Özyilmaz B and Castro Neto A H 2014 Scattering theory of spin-orbit active adatoms on graphene *Phys. Rev. X* **90** 035444
- [29] Brey L 2015 Spin-orbit coupling in graphene induced by adatoms with outer-shell *p* orbitals *Phys. Rev. B* **92** 235444

- [30] Pratontep S, Carroll S J, Xirouchaki C, Streun M and Palmer R E 2005 Size-selected cluster beam source based on radio frequency magnetron plasma sputtering and gas condensation *Rev. Sci. Instrum.* **76** 045103
- [31] Liao T 2018 Production and characterization of novel catalysts based on bimetallic deposited clusters *PhD Thesis* KU Leuven
- [32] Cox A J, Louderback J G and Bloomfield L A 1993 Experimental observation of magnetism in rhodium clusters *Phys. Rev. Lett.* **71** 923–6
- [33] Janssens E, Le H T and Lievens P 2015 Adsorption of propene on neutral gold clusters in the gas phase *Chem. Eur. J.* **21** 15256–62
- [34] Haruta M 1997 Size- and support-dependency in the catalysis of gold *Catal. Today* **36** 153–66
- [35] Woodham A P, Meijer G and Felicke A 2013 Charge separation promoted activation of molecular oxygen by neutral gold clusters *J. Am. Chem. Soc.* **135** 1727–30
- [36] Castleman A W 2011 From elements to clusters: the periodic table revisited *J. Phys. Chem. Lett.* **2** 1062–9
- [37] Scheerder J E, Picot T, Reckinger N, Sneyder T, Zharinov V S, Colomer J-F, Janssens E and Van de Vondel J 2017 Decorating graphene with size-selected few-atom clusters: a novel approach to investigate graphene–adparticle interactions *Nanoscale* **9** 10494–501
- [38] Scheerder J E, Liu S, Zharinov V S, Reckinger N, Colomer J-F, Cheng H, Van de Vondel J and Janssens E 2018 Electronic detection of oxygen adsorption and size-specific doping of few-atom gold clusters on graphene *Adv. Mater. Interfaces* **5** 1801274
- [39] Rashba E I 2000 Theory of electrical spin injection: tunnel contacts as a solution of the conductivity mismatch problem *Phys. Rev. B* **62** 267–70
- [40] Han W, McCreary K M, Pi K, Wang W H, Li Y, Wen H, Chen J R and Kawakami R K 2012 Spin transport and relaxation in graphene *J. Magn. Magn. Mater.* **324** 369–81
- [41] Novoselov K S, Geim A K, Morozov S V, Jiang D, Zhang Y, Dubonos S V, Grigorieva I V and Firsov A A 2004 Electric field effect in atomically thin carbon films *Science* **306** 666–9
- [42] Verguts K, Defossez Y, Leonhardt A, De Messemaeker J, Schouteden K, Van Haesendonck C, Huyghebaert C, De Gendt S and Brems S 2018 Growth of millimeter-sized graphene single crystals on Al₂O₃ (0001)/Pt(111) template wafers using chemical vapor deposition *ECS J. Solid State Sci. Technol.* **7** M195–200
- [43] Chen J H, Jang C, Adam S, Fuhrer M S, Williams E D and Ishigami M 2008 Charged-impurity scattering in graphene *Nat. Phys.* **4** 377–81
- [44] Dorgan V E, Bae M-H and Pop E 2010 Mobility and saturation velocity in graphene on SiO₂ *Appl. Phys. Lett.* **97** 082112
- [45] Johnson M and Silsbee R H 1988 Coupling of electronic charge and spin at a ferromagnetic-paramagnetic metal interface *Phys. Rev. B* **37** 5312–25
- [46] Johnson M and Silsbee R H 2007 Calculation of nonlocal baseline resistance in a quasi-one-dimensional wire *Phys. Rev. B* **76** 153107
- [47] Volmer F, Drögeler M, Pohlmann T, Güntherodt G, Stampfer C and Beschoten B 2015 Contact-induced charge contributions to non-local spin transport measurements in co/MgO/graphene devices *2D Mater.* **2** 024001
- [48] Han W, Pi K, McCreary K M, Li Y, Wong J J I, Swartz A G and Kawakami R K 2010 Tunneling spin injection into single layer graphene *Phys. Rev. Lett.* **105** 167202
- [49] Tan Y W, Zhang Y, Bolotin K, Zhao Y, Adam S, Hwang E H, Das Sarma S, Stormer H L and Kim P 2007 Measurement of scattering rate and minimum conductivity in graphene *Phys. Rev. Lett.* **99** 246803
- [50] Plant S R, Cao L, Yin F, Wang Z W and Palmer R E 2014 Size-dependent propagation of Au nanoclusters through few-layer graphene *Nanoscale* **6** 1258–63
- [51] Pi K, McCreary K M, Bao W, Wei Han Y F, Chiang Y Li, Tsai S W, Lau C N and Kawakami R K 2009 Electronic doping and scattering by transition metals on graphene *Phys. Rev. B* **80** 075406
- [52] Adam S, Hwang E H, Galitski V M and Das Sarma S 2007 A self-consistent theory for graphene transport *Proc. Natl Acad. Sci.* **104** 18392–7
- [53] Takahashi S and Maekawa S 2003 Spin injection and detection in magnetic nanostructures *Phys. Rev. B* **67** 052409
- [54] Kresse G and Hafner J 1993 *Ab initio* molecular dynamics for liquid metals *Phys. Rev. B* **47** 558–61
- [55] Kresse G and Furthmüller J 1996 Efficiency of *ab-initio* total energy calculations for metals and semiconductors using a plane-wave basis set *Comput. Mater. Sci.* **6** 15–50
- [56] Kresse G and Joubert D 1999 From ultrasoft pseudopotentials to the projector augmented-wave method *Phys. Rev. B* **59** 1758–75
- [57] Blöchl P E 1994 Projector augmented-wave method *Phys. Rev. B* **50** 17953–79
- [58] Marchenko D, Varykhalov A, Scholz M R, Bihlmayer G, Rashba E I, Rybkin A, Shikin A M and Rader O 2012 Giant Rashba splitting in graphene due to hybridization with gold *Nat. Commun.* **3** 1232
- [59] Ma D, Li Z and Yang Z 2012 Strong spin–orbit splitting in graphene with adsorbed Au atoms *Carbon* **50** 297–305
- [60] Varykhalov A, Sánchez-Barriga J, Shikin A M, Biswas C, Vescovo E, Rybkin A, Marchenko D and Rader O 2008 Electronic and magnetic properties of quasifreestanding graphene on Ni *Phys. Rev. Lett.* **101** 157601
- [61] Elliott R J 1954 Theory of the effect of spin-orbit coupling on magnetic resonance in some semiconductors *Phys. Rev.* **96** 266–79
- [62] Yafet Y 1952 Calculation of the g factor of metallic sodium *Phys. Rev.* **85** 478
- [63] Ochoa H, Castro Neto A H and Guinea F 2012 Elliott–Yafet mechanism in graphene *Phys. Rev. Lett.* **108** 206808